Influence of coherent Raman scattering on coherent population trapping in atomic sodium vapor

Vincent Wong,* Ryan S. Bennink, Alberto M. Marino, Robert W. Boyd, and C. R. Stroud, Jr.
The Institute of Optics, University of Rochester, Rochester, New York 14627, USA

F. A. Narducci
EO Sensors Division, Naval Air Systems Command, Patuxent River, Maryland 20670, USA
(Received 7 May 2004; published 11 November 2004)

We study how coherent Stokes and anti-Stokes Raman scattering influence coherent population trapping. In an experiment using an atomic sodium vapor cell we observe induced transparency, induced absorption, and gain features, all of subnatural linewidth. The electromagnetically induced resonance is a peak or a dip depending on which side of the optical transition the fields are tuned to, and thus whether coherent anti-Stokes Raman scattering or coherent Stokes Raman scattering is the dominant process.

DOI: 10.1103/PhysRevA.70.053811 PACS number(s): 42.50.Gy, 42.65.Dr, 32.80.Qk, 33.40.+f

I. INTRODUCTION

Coherent population trapping (CPT) [1–3] and electromagnetically induced transparency (EIT) [4,5] have been studied extensively in recent years and have given rise to many exciting applications. Although both processes create a transparency window, there are subtle differences. CPT only occurs in a Λ system and utilizes comparable field strengths. It was shown in early work that EIT can be used to enhance the efficiency of the process of third-order sum-frequency mixing [4]. CPT has also been shown to enhance other nonlinear effects such as coherent Raman scattering [6–9]. CPT has more recently been used for velocity-selective laser cooling [10], and the generation of slow light [11,12] as a consequence of the rapid variation of the refractive index associated with the transparency window. The CPT resonance can also be used as a spectroscopic tool [13] and even as a frequency reference [13–15] because of the narrow resonance width.

An effect opposite to CPT or EIT is electromagnetically induced absorption (EIA), which has also been observed. There are two different processes that have been shown to lead to EIA: (i) spontaneous coherence transfer in a degenerate two-level system [16–18], and (ii) three-photon transitions in a quasidegenerate *N*-level configuration [19,20] which involves a four wave mixing process. In the presence of EIA, the generation of fast light [21] becomes possible. At high intensities, Zibrov and co-workers [19] have observed an EIT resonance inside the EIA feature and Babin *et al.* [22] have observed splitting of the EIT resonance in a Λ system.

Despite the extensive previous work on EIT and CPT, the influence of Raman scattering on CPT has seldom been discussed. Coherent Raman scattering [23–26] has been widely used as a tool for spectroscopy. Examples of coherent Raman scattering are coherent anti-Stokes Raman scattering (CARS) [27–29] and its counterpart, coherent Stokes Raman scattering (CSRS). There is also a variety of different geometries (collinear, boxcar [30], etc.) for achieving phase matching. For certain collinear CARS or CSRS, phase matching is not perfect but the overlap region is longer than in noncollinear coherent Raman scattering, which might be desirable for certain applications.

The process of molecular coherent Raman scattering involves two applied fields (ν_1 and ν_2) which are tuned to excite a vibrational or rotational mode. A third applied field (ν_3) can then scatter off this coherently prepared medium and gain (or lose) energy from (to) the vibrational mode to generate the anti-Stokes (Stokes) idler field. When $\nu_1 > \nu_2$ ($\nu_1 < \nu_2$) and $\nu_1 = \nu_3$, this interaction is known as CARS (CSRS). Traditionally, CARS and CSRS operate far away from a single-photon resonance. If the fields are tuned close to the optical transition, the idler can be enhanced and the excited state properties can be studied too, as in resonance Raman scattering [31]. In an atomic system, we create a ground-state (spin) or quantum-superposition coherence instead of exciting a vibrational mode. Since the decoherence rate between the hyperfine ground levels is very low, we can obtain very narrow and strong features on both the idler and applied fields. Such a process utilizes the same quantum coherence that is responsible for CPT.

In this paper, we analyze how coherent Raman scattering affects CPT. In the next section, we present experimental results showing both CPT and EIA along with gain in the Doppler-broadened spectrum and show how CARS and CSRS coexist with CPT and lead to EIA. We also give an intuitive explanation via an energy level diagram that depicts the ongoing process. This is followed by a description of a more detailed theoretical three-level model involving six waves.

II. EXPERIMENT

The experimental layout is depicted in Fig. 1. The experiment is performed with a continuous-wave dye laser whose output is split into two beams, and the polarization of one of the beams is rotated such that the two beams are of linear and mutually orthogonal polarization. The vertically polarized beam is double-passed through a variable-frequency acousto-optic modulator (AOM) with a center frequency of +80

*Electronic address: vin@optics.rochester.edu

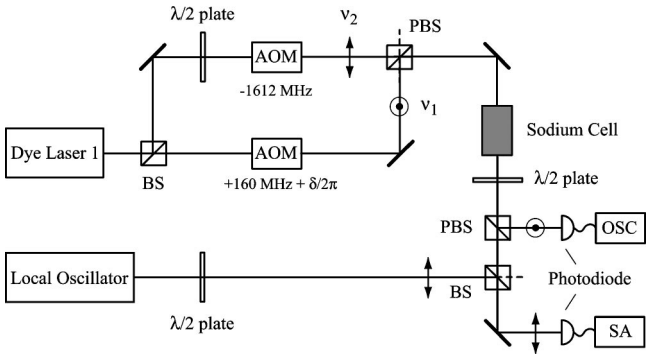

FIG. 1. Experimental layout. ⊙ indicates vertical polarization, and ↔ indicates horizontal polarization. AOM, acousto-optic modulator; PBS, polarizing beam splitter; BS, beam splitter; λ/2 plate, half-wave plate; OSC, oscilloscope; SA, spectrum analyzer. ν_1 is generated by a variable frequency AOM. The output from a second dye laser is used as a local oscillator in a heterodyne detection setup for determining the frequency content of the transmitted field. The half-wave plate and polarizing beam splitter (after the cell) are used to select which polarization component of the beam is mixed with the local oscillator.

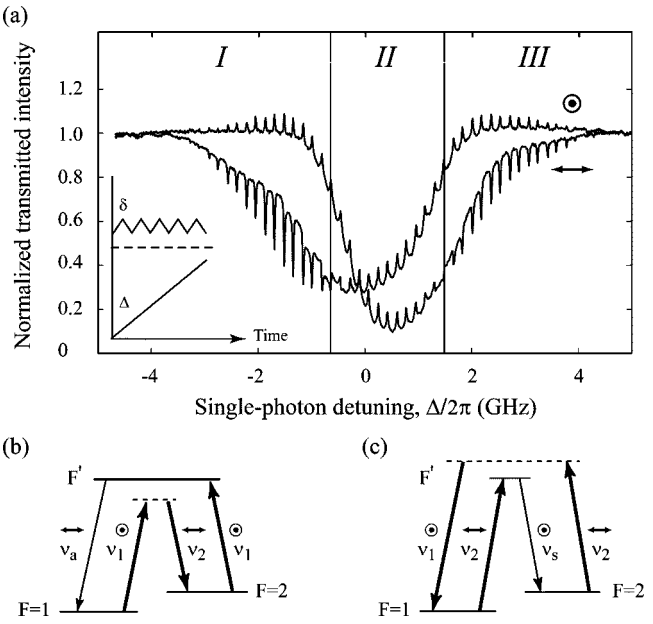

FIG. 2. (a) Dual-scan experimental transmission spectrum of each polarization component showing electromagnetically induced absorption, induced transparency, and gain. Inset: Timing diagram of the detuning scans: Raman detuning $(\delta/2\pi)$ and single-photon detuning $(\Delta/2\pi)$. (b) Energy level diagram for red-detuned pump fields (region I) depicting CARS as the dominant process. This process pumps energy from the vertical polarization to the horizontal polarization, leading to induced absorption for the vertical polarization and induced transmission and gain for the horizontal polarization. (c) Energy level diagram with blue-detuned pump fields (region III) depicting CSRS as the dominant process. In this case, energy is pumped from the horizontal polarization to the vertical polarization, leading to induced absorption for the horizontal polarization and induced transmission and gain for the vertical polarization.

MHz to vary the detuning $(\delta/2\pi)$ around the Raman resonance. The frequency of this beam (ν_1) is nominally resonant with the transition between the $F=1$ ground level and the unresolved excited levels (F') of the sodium $D1$ line. The horizontally polarized beam is passed through a fixed frequency $(-1612$ MHz) AOM to down-shift the frequency of the beam. The frequency of this second beam (ν_2) is nominally resonant with the transition involving the $F=2$ ground level. The separation of the hyperfine ground levels of atomic sodium is 1772 MHz. The separation of the hyperfine excited levels is smaller than the Doppler width, and therefore the levels are unresolvable in the current experimental configuration. These pump beams are combined using a polarizing beam splitter and directed into a sodium vapor cell. The power of each collimated beam going into the cell is 15 mW with a $1/e$ intensity diameter of 4 mm.

The vapor cell is shielded with a mu-metal case to reduce stray magnetic fields. The cell is filled with 0.4 torr of helium (see end of this section) and heated to 150 °C producing a number density of 10^{11} atoms/cm^3. After propagation through the 7-cm-long vapor cell, the beams are separated with a second polarizing beam splitter, detected with photodiodes, and monitored with an oscilloscope. A second dye laser is used as a local oscillator in a heterodyne detection setup to determine the frequency of any generated field. A second halfwave plate together with the polarizing beam splitter (after the cell) are used to select which polarization component is mixed with the local oscillator and sent to the spectrum analyzer. Note that any designation of field polarization refers to that of the beam before and in the cell, since the portion of the beam that is sent to the spectrum analyzer is always horizontally polarized to enable mixing with the local oscillator beam.

Our measurement procedure is illustrated schematically in the inset of Fig. 2(a). We dither the Raman detuning $(\delta/2\pi)$ rapidly as the single-photon detuning $(\Delta/2\pi)$ is scanned slowly across the Doppler profile. The single-photon detunings of both beams are scanned by varying the frequency of the dye laser, whereas the Raman detuning is varied with the AOM. This dual-scan technique allows us to observe the Raman atomic response as we tune across the Doppler profile. There are three regions in the observed transmission spectra of Fig. 2(a). In region I, induced absorption of the vertically polarized component is observed when the frequency difference between the two pump fields is tuned to the Raman resonance; the other component experiences increased transmission and even gain (note that the signal is larger than the far-off-resonance background). In region II, both beams experience induced transparency. In region III, induced absorption is observed for the horizontally polarized beam and increased transmission and gain is observed for the vertically polarized beam. In the transition areas between these regions [near the two vertical bars in Fig. 2(a)], the spectra have a dispersive-like profile. This is due to competition between the gain and absorption processes.

The underlying physical process giving rise to the rich spectral behavior of Fig. 2(a) is coherent Raman scattering. The energy-level diagram of Fig. 2(b) depicts CARS, which is the dominant process in region I. The vertically polarized

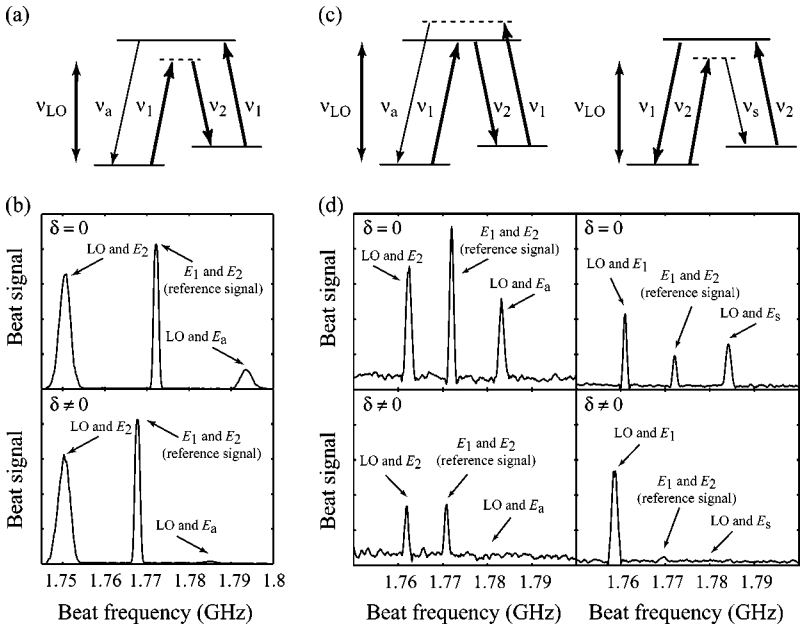

FIG. 3. (a) Energy level diagram depicting CARS with red-deturned pump fields (region I). The local oscillator is tuned near ν_1. (b) The beat signals are of the horizontally polarized fields when the two pump fields are on ($\delta=0$) and off ($\delta\neq 0$) the Raman resonance. The beat signals are plotted on a linear vertical scale. (c) Energy level diagrams showing CARS on the left and CSRS on the right which occur simultaneously when the pump fields are tuned near the single-photon resonance (region II). The local oscillator is tuned near the frequency of the pump field that contributed 2 photons. (d) The beat signal of the horizontally (vertically)-polarized fields shows the presence of the CARS (CSRS) idler field.

field ν_1 acts as an energy source which contributes two photons to amplify the horizontally polarized field ν_2 and create an anti-Stokes photon which is also horizontally polarized. Figure 2(c) depicts CSRS, which is the dominant process in region III. In this region, the fields ν_1 and ν_2 swap roles as the energy source and recipient, and we see an increase in the number of vertically polarized photons. In region II, both CARS and CSRS occur with comparable strength which leads to a cancellation of the number of photons absorbed from and emitted into each polarization component. Because of this cancellation, the transmission peaks observed in each polarization component occur entirely as a consequence of conventional CPT. We know that both CARS and CSRS occur simultaneously in this region because both Stokes and anti-Stokes frequency components are observable in the transmitted fields, as we demonstrate next.

We confirmed the presence of the idler field by performing a heterodyne measurement of the frequency content of the beam emerging from the sodium cell. The frequency (ν_{LO}) of the local oscillator used in this measurement is tuned to approximately ν_1-20 MHz as shown in Fig. 3(a). Figure 3(b) shows the heterodyne signal of the horizontally polarized component for frequencies near the difference frequency (1772 MHz) of the two pump fields (E_1 and E_2), which are red-detuned from the optical resonance (region I). The central peak of this spectrum is a reference signal representing the beat note between the two pump frequencies. This signal is present because of uncompensated birefringence in the sapphire windows of the vapor cell, which tends to mix the two initially orthogonal polarization components. This peak also has a small contribution from the beat note of E_1 and the generated field E_a. The leftmost peak in the spectrum is the beat signal between the local oscillator and E_2. The rightmost peak is the beat note between the local oscillator and the generated anti-Stokes field; this contribution is greatly diminished when the two pump fields are detuned from the Raman resonance. The pump fields are tuned off the Raman resonance by shifting ν_1 (while holding ν_2 fixed), which causes the positions of the other two peaks to shift. The outer peaks are broader than the reference peak because the two dye lasers are not phase-locked; consequently the beat frequency fluctuates. CSRS is also present but much weaker and the CSRS signal is on the vertically polarized component of the beam and far off resonance with the beat note at 2×1772 MHz.

The beat-note spectrum (not shown) for blue-detuned pump fields (region III) have a similar appearance. The generated Stokes signal is vertically polarized and the beat note of the Stokes signal is observed (around 1772 MHz) by heterodyning the vertically polarized component of the beam with a local oscillator tuned near ν_2.

When the pump fields are tuned near the single-photon resonance (region II) both CARS and CSRS processes influence the transmitted beam. The frequency of the local oscillator is tuned to approximately ν_1-10 MHz for observing the CARS signal and approximately ν_2+10 MHz for observing the CSRS signal, as shown in Fig. 3(c). CARS (CSRS) generates a horizontally (vertically) polarized idler field which can be observed in the beat signal spectrum of the horizontally (vertically) polarized beam with the pump fields on Raman resonance [Fig. 3(d)]. These traces are noisier than those of Fig. 3(b) because less signal averaging was used in the present case.

The relative heights of the peaks in the beat-note spectra can be misleading; the left peak of Fig. 3(b) is taller than the right peak because the field at frequency ν_2 experiences less absorption and therefore is much stronger (at the exit window of the cell) than any of the other fields. In Fig. 3(d), the reference and leftmost peaks become smaller when the pump fields are tuned away from the Raman resonance. This occurrence is due to the reduction of CPT in the off-Raman resonance condition while the pump fields are tuned near the peak of the Doppler absorption profile.

The scattering efficiency is fairly large, $\lesssim$40%, as deduced from the dip of the spectrum in region I of Fig. 2(a). In the presence of background absorption, not every scattered

photon is detected. Therefore, the scattering efficiency is not calculated using the peaks.

In an EIT configuration where one of the pump fields is stronger than the other pump field, the idler signal will be correspondingly weaker. This is due to the reduction of the ground state coherence with unbalanced pump field strengths. When the intensity of the pump field contributing two photons is reduced, not only is the ground state coherence decreased, the probe intensity is also decreased thereby weakening the scattered signal.

We have also repeated these experiments without any buffer gas in the cell and have observed similar spectra but with slightly reduced peak heights. This result shows that pressure broadening is not required for the occurrence of these Raman scattering processes. We have also varied the amount and type of buffer gas. We find that for all of the buffer gases used (helium, argon, and nitrogen), the resonances are narrowed and the Raman scattering processes are enhanced as the buffer gas pressure is increased up to a value of a few torr. This behavior is due to the reduction of the ground state decoherence rate which, in this regime, is determined by the diffusion of sodium atoms out of the laser beam. Upon increasing the buffer gas pressure still further, all the resonances were found to weaken. In this regime pressure broadening of the optical resonance becomes important, and the saturation intensity increases with buffer gas pressure. For the laser intensities we used, the Rabi frequency is not large enough to create a significant amount of ground state coherence. This trend was also observed in our numerical simulations.

III. THEORY

When two applied fields (which we call the pump fields) are tuned to the Raman resonance of a Λ system, the probability amplitudes for excitation to the upper level cancel as a consequence of quantum interference. A coherence between the two ground states, or equivalently a dark state [1], is thus created. In addition to providing transparency for both fields, we can utilize this coherence for the generation of an idler field by scattering a third (probe) field off this coherence. Based on energy conservation, the frequency of the idler field differs from that of the third field by the frequency difference of the two pump fields that created the coherence. However, this scattering process transfers population from one of the lower levels to the other, thus upsetting the original dark state. Absorption of additional photons out of the pump fields is necessary for reestablishing this dark state.

Although the $D1$ line of sodium couples 16 different hyperfine Zeeman levels [32], we will approximate it with a three-level Λ system. This simplification will lead to some discrepancies that are discussed at the end of this section.

In our model, we let each of the two applied fields, ω_1 and ω_2, couple to both optical transitions of the Λ system. The ω_1 field is tuned near the a-c transition and acts as a pump field for this transition. Likewise, the ω_2 field is tuned near the b-c transition and acts as a pump field for this transition. Since ω_1 is off resonance for the b-c transition, it serves as a probe field for this transition, and leads to the generation of light at the anti-Stokes frequency. Likewise ω_2 serves as a probe field for the a-c transition and leads to the generation of light at the Stokes frequency. This circumstance is illustrated in Fig. 4, which shows the Λ system with the six field contributions. The subscript "v" ("h") indicates vertical (horizontal) polarization of the applied field. The subscript "a" ("s") indicates the generated anti-Stokes (Stokes) field which is not applied. The fields are defined as

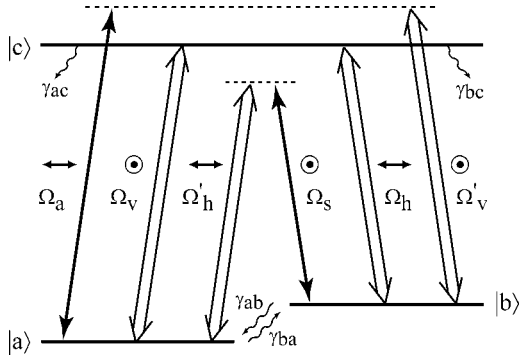

FIG. 4. Energy level diagram of the six-wave three-level Λ system used in the theoretical model. Ω_v (Ω_h) is the Rabi frequency of the primary contribution of the vertically (horizontally) polarized applied field. Ω_v' and Ω_h' indicate the secondary contributions. Note that the frequencies obey $\omega_{\rm v}=\omega_{\rm v}'=\omega_1$ and $\omega_{\rm h}=\omega_{\rm h}'=\omega_2$. Ω_a ($\Omega_{\rm s}$) is the anti-Stokes (Stokes) idler field that is generated.

$$\tilde{E}(t) = (E_1 + E_{\rm a}e^{-i\beta t})e^{-i\omega_1 t} + (E_{\rm s}e^{i\beta t} + E_2)e^{-i\omega_2 t} + \text{c.c.}, \quad (1)$$

where $\beta=\omega_1-\omega_2$. ω_1 is varied to change the Raman detuning, $\delta=\Delta_1-\Delta_2=\beta-(2\pi\times 1772\ \text{MHz})$, where $\Delta_1=\omega_1-\omega_{\rm ca}$ and $\Delta_2=\omega_2-\omega_{\rm cb}$. The labels with and without the prime ($'$) indicate primary (pump) and secondary (probe) contributions of the applied fields, respectively. The terms *pump* and *probe* are used only to distinguish between the two contributions of a particular applied field. Note that although $E_{\rm v}=E_{\rm v}'$, the effective Rabi frequencies, $\Omega_{\rm v,eff}(\Delta_1,\mu_{\rm ca})$ and $\Omega_{\rm v,eff}'(\Delta_1+\beta,\mu_{\rm cb})$, need not be equal because the detunings and the dipole matrix elements μ_{ij} of the respective transitions are not equal. Nonetheless, the dipole matrix elements of the two optical transitions are of the same order of magnitude. Consistent with the notation used in the previous section, $\omega_{\rm v}=\omega_{\rm v}'=\omega_1$ and $\omega_{\rm h}=\omega_{\rm h}'=\omega_2$, but we have used angular frequencies exclusively for this and subsequent sections.

We formulate the density-matrix equations of motion and perform a rotating frame transformation. Using the rotating-wave approximation, we obtain the equations of motion as shown in Appendix A. We then use the population conservation to eliminate $\sigma_{\rm cc}$ from the equations and write them in matrix form as

$$-\dot{R} + BR = S, \quad (2)$$

where R is the column vector

$$R \equiv [\sigma_{\rm aa}\ \sigma_{\rm bb}\ \sigma_{\rm ba}\ \sigma_{\rm ca}\ \sigma_{\rm cb}\ \sigma_{\rm ab}\ \sigma_{\rm ac}\ \sigma_{\rm bc}]^{\rm T}, \quad (3)$$

the matrix B consists of the Hamiltonian and decay terms, and the vector S is the driving term of the differential equation. The driving term results from our incorporation of the

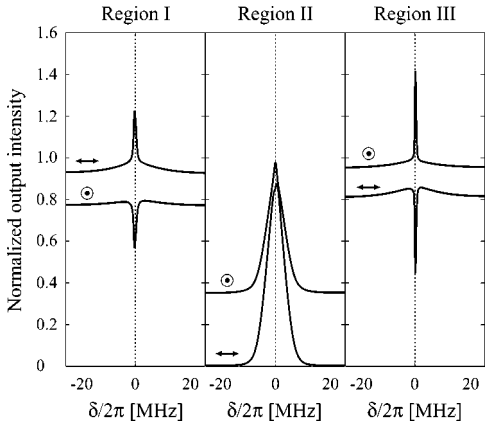

FIG. 5. Theoretical spectra of the intensities of the two polarization components as a function of the Raman detuning (δ) for the three different regions of pump field detuning from the optical transition.

conservation of probability. R can be solved (to all orders of the field strength) using the Fourier expansion and continued fraction method as outlined in Appendix B. The material response is Doppler averaged, and the fields are propagated using the reduced wave equation

$$\frac{dE_j(\omega_j,z)}{dz} = i2\pi k_j P_j(\omega_j,z), \tag{4}$$

where E is the electric field, P is the Fourier component of the calculated atomic polarization, k is the wave vector, and $j=1$, 2, a, or s. We have used the slowly-varying amplitude approximation and assumed no transverse effects.

Figure 5 shows the output intensities of the vertically and horizontally polarized components versus the Raman detuning δ for the three regions studied: region I, red detuned pump fields ($\Delta=-\beta$); region II, pump fields tuned near to the resonance of the optical transitions ($\Delta=0$); and region III, blue detuned pump fields ($\Delta=\beta$).

Figure 6 shows the calculated ground state coherence $|\sigma_{ba}|$ after propagation. The dashed curve is with only CPT, and the solid curve is with both CPT and coherent Raman scattering processes present in the system. The CPT-only response is obtained by using only the zeroth Floquet order in the simulation. For CPT only, in an ideal homogeneously broadened system without propagation, the one-photon-resonant ground state coherence has a maximal value of 0.5, which decreases significantly when the fields are far detuned from the optical resonance. In region II, the peak coherence is slightly reduced when coherent Raman scattering is involved. However, in regions I and III, the peak coherence is actually increased. This is not too surprising as Raman scattering is known to create coherence. The spectra in those regions are also somewhat asymmetric and shifted. With the inclusion of coherent Raman scattering, even the spectrum in region II experiences a Stark-like shift.

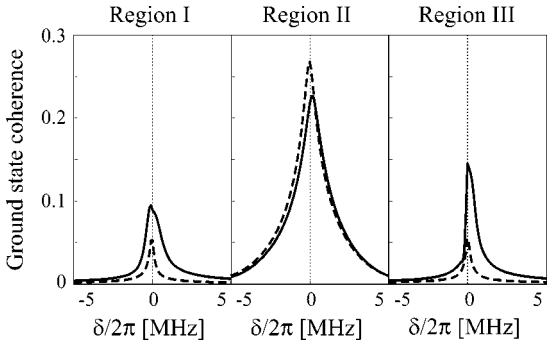

FIG. 6. Theoretical spectra of the magnitude of the ground state coherence $|\sigma_{ba}|$ after propagation for the 3 regions studied. The dash curve is with only CPT present while the solid curve includes both CARS and CSRS processes.

The model also takes into account the possibility of interference between the CARS process and the CSRS process. Additionally, nonparametric six-wave mixing processes are also accounted for.

The numerical results agree qualitatively with the experiment. The nonperfect transparency of the CPT resonances is due to a variety of less important experimental imperfections that result in weaker resonances due to additional absorption. For example, the 80 MHz AOM introduces sidebands which reduces the coherence between the ground states. The cleanliness of the sodium cell and purity of the buffer gases used also affects the amount of additional stray absorption that is introduced. The simplification of the theoretical model of sodium also fails to take into account other less significant but concurrent processes that exist in the real system. When the second hyperfine excited level, or the Zeeman structure [32] is taken into account, even if they are degenerate, the CPT resonance will appear weaker, as discussed in [33].

IV. CONCLUSION

We have studied coherent Raman scattering and its influence on coherent population trapping in a low-density atomic sodium vapor. The transmission spectra of the applied laser fields possess features having subnatural linewidths as a consequence of the quantum coherence of the underlying physical processes. An interplay between the Raman scattering processes and CPT is observed. When Raman scattering dominates, the usual CPT transparency peak can become inverted leading to EIA. These coherent Raman processes in addition to CPT are present across the entire Doppler profile. We have also verified the presence of the Stokes and anti-Stokes idler signals using a heterodyne detection setup. These results can be understood conceptually in terms of models based on simple energy-level diagrams and can be understood more formally in terms of a density matrix calculation based on a six-wave three-level Λ model.

ACKNOWLEDGMENTS

This work is supported by the Office of Naval Research under Grant No. N00014-02-1-0797 and the Department of Energy under Grant No. DE-FG02-01ER15156. F.A.N. would also like to acknowledge support from the Office of Naval Research and the Naval Air Systems Command.

APPENDIX A: DENSITY MATRIX EQUATIONS OF MOTION

We begin with the standard density matrix equations of motion for the three-level Λ system. We perform a rotating-frame transformation using

$$\rho_{ca} = \sigma_{ca} e^{-i\omega_1 t}, \tag{A1a}$$

$$\rho_{cb} = \sigma_{ca} e^{-i\omega_2 t}, \tag{A1b}$$

$$\rho_{ba} = \sigma_{ba} e^{-i(\omega_1-\omega_2)t}, \tag{A1c}$$

and make a rotating-wave approximation to obtain the density matrix equations of motion for the six-wave mixing process as follows:

$$\dot{\sigma}_{aa} = \frac{i}{2}(\Omega_1^* + \Omega_3^* e^{-i\beta t})\sigma_{ca} - \frac{i}{2}(\Omega_1 + \Omega_3 e^{i\beta t})\sigma_{ac} - \gamma_{ba}\sigma_{aa} + \gamma_{ab}\sigma_{bb} + \gamma_{ac}\sigma_{cc}, \tag{A2a}$$

$$\dot{\sigma}_{bb} = \frac{i}{2}(\Omega_2^* + \Omega_4^* e^{i\beta t})\sigma_{cb} - \frac{i}{2}(\Omega_2 + \Omega_4 e^{-i\beta t})\sigma_{bc} + \gamma_{ba}\sigma_{aa} - \gamma_{ab}\sigma_{bb} + \gamma_{bc}\sigma_{cc}, \tag{A2b}$$

$$\dot{\sigma}_{cc} = -\frac{i}{2}(\Omega_1^* + \Omega_3^* e^{-i\beta t})\sigma_{ca} + \frac{i}{2}(\Omega_1 + \Omega_3 e^{i\beta t})\sigma_{ac} - \frac{i}{2}(\Omega_2^* + \Omega_4^* e^{i\beta t})\sigma_{cb} + \frac{i}{2}(\Omega_2 + \Omega_4 e^{-i\beta t})\sigma_{bc} - (\gamma_{ac} + \gamma_{bc})\sigma_{cc}, \tag{A2c}$$

$$\dot{\sigma}_{ba} = i(\Delta_{ba} + i\Gamma_{ba})\sigma_{ba} + \frac{i}{2}(\Omega_2^* + \Omega_4^* e^{i\beta t})\sigma_{ca} - \frac{i}{2}(\Omega_1 + \Omega_3 e^{i\beta t})\sigma_{bc}, \tag{A2d}$$

$$\dot{\sigma}_{ca} = i(\Delta_{ca} + i\Gamma_{ca})\sigma_{ca} + \frac{i}{2}(\Omega_1 + \Omega_3 e^{i\beta t})\sigma_{aa} - \frac{i}{2}(\Omega_1 + \Omega_3 e^{i\beta t})\sigma_{cc} + \frac{i}{2}(\Omega_2 + \Omega_4 e^{-i\beta t})\sigma_{ba}, \tag{A2e}$$

$$\dot{\sigma}_{cb} = i(\Delta_{cb} + i\Gamma_{cb})\sigma_{cb} + \frac{i}{2}(\Omega_2 + \Omega_4 e^{-i\beta t})\sigma_{bb} - \frac{i}{2}(\Omega_2 + \Omega_4 e^{-i\beta t})\sigma_{cc} + \frac{i}{2}(\Omega_1 + \Omega_3 e^{i\beta t})\sigma_{ab}, \tag{A2f}$$

$$\dot{\sigma}_{ab} = -i(\Delta_{ab} - i\Gamma_{ab})\sigma_{ab} - \frac{i}{2}(\Omega_2 + \Omega_4 e^{-i\beta t})\sigma_{ac} + \frac{i}{2}(\Omega_1^* + \Omega_3^* e^{-i\beta t})\sigma_{cb}, \tag{A2g}$$

$$\dot{\sigma}_{ac} = -i(\Delta_{ac} - i\Gamma_{ac})\sigma_{ac} - \frac{i}{2}(\Omega_1^* + \Omega_3^* e^{-i\beta t})\sigma_{aa} + \frac{i}{2}(\Omega_1^* + \Omega_3^* e^{-i\beta t})\sigma_{cc} - \frac{i}{2}(\Omega_2^* + \Omega_4^* e^{i\beta t})\sigma_{ab}, \tag{A2h}$$

$$\dot{\sigma}_{bc} = -i(\Delta_{bc} + i\Gamma_{bc})\sigma_{bc} - \frac{i}{2}(\Omega_2^* + \Omega_4^* e^{i\beta t})\sigma_{bb} + \frac{i}{2}(\Omega_2^* + \Omega_4^* e^{i\beta t})\sigma_{cc} - \frac{i}{2}(\Omega_1^* + \Omega_3^* e^{-i\beta t})\sigma_{ba}. \tag{A2i}$$

APPENDIX B: FLOQUET EXPANSION AND THE CONTINUED FRACTION

The equations of motion can be solved for all their harmonic terms using Floquet's theorem as is done in [34] but with a slight modification because the driving term (S) of the differential equation [Eq. (2)] has harmonic content. We expand each term in the equations of motion accordingly as

$$S = S_{-1} e^{i\beta t} + S_0 + S_1 e^{-i\beta t}, \tag{B1}$$

$$B = B_{-1} e^{i\beta t} + B_0 + B_1 e^{-i\beta t}, \tag{B2}$$

$$R = \ldots + R_{-3} e^{i3\beta t} + R_{-2} e^{i2\beta t} + R_{-1} e^{i\beta t} + R_0 + R_1 e^{-i\beta t} + R_2 e^{-i2\beta t} + R_3 e^{-i3\beta t} + \ldots . \tag{B3}$$

We can then write the recurrence relation for the harmonic terms of R as

$$B_1 R_{q-1} + A_q R_q + B_{-1} R_{q+1} = S_q, \tag{B4}$$

where $A_q = B_0 + (iq\beta)$.

Multiplying both sides by A_q^{-1}, Eq. (B4) becomes

$$C_q R_{q-1} + R_q + G_q R_{q+1} = S_q, \tag{B5}$$

where

$$C_q = A_q^{-1} B_1, \tag{B6}$$

$$G_q = A_q^{-1} B_{-1}, \tag{B7}$$

$$b_q = A_q^{-1} S_q, \tag{B8}$$

and b_q is nonzero only for $q=0, \pm 1$.

Solving the continued fraction of Eq. (B5), we truncate the expansion to a large index Q such that $R_Q=0$ for $q>Q$. We then iteratively eliminate R_Q, R_{Q-1} and so on using $R_Q = -C_Q R_{Q-1}$ until we reach the relation for $q=2$,

$$R_2 = -(I - G_2[I - G_3\{\ldots G_{Q-1}(I - G_{Q-1}C_Q)^{-1} \times C_{Q-1}\ldots\}^{-1}C_4]^{-1}C_3)^{-1}C_2 R_1, \tag{B9}$$

where I is the identity matrix. Let us define everything to the left of R_1 in the above equation as N^+ so that

$$R_2 = N^+ R_1. \tag{B10}$$

Since b_1 is nonzero, the relation between R_1 and R_0 has an additional term (b_1),

$$R_1 = (I + G_1 N^+)^{-1} b_1 - (I + G_1 N^+)^{-1} C_1 R_0, \tag{B11}$$

$$R_1 = -Y^+ b_1 + M^+ R_0, \tag{B12}$$

where Y^+ is related to M^+ by $M^+ = Y^+ C_1$. In the absence of b_1, we have just the second term in Eq. (B12) (as obtained by the iterative method to $q=1$). Repeating the procedure for $q=-Q$, we obtain

$$R_{-1} = -Y^- b_{-1} + M^- R_0, \tag{B13}$$

where

$$Y^- = -(I - C_{-1}[I - C_{-2}\{\ldots C_{-Q+2}(I - C_{-Q+1}G_{-Q})^{-1} \times G_{-Q+1}\ldots\}^{-1}G_{-3}]^{-1}G_{-2})^{-1}, \tag{B14}$$

and $M^- = Y^- G_{-1}$. For the $q=0$ term, we substitute R_{-1} and R_1 into Eq. (B5) and obtain

$$R_0 = (I + C_0 M^- + G_0 M^+)^{-1} C_0 Y^- b_{-1} + (I + C_0 M^- + G_0 M^+)^{-1} G_0 Y^+ b_1 + (I + C_0 M^- + G_0 M^+)^{-1} b_0. \tag{B15}$$

R_1 and R_{-1} are calculated using Eqs. (B12) and (B13), respectively. R_2 can then be calculated using Eq. (B10) and R_{-2} from the equivalent of Eq. (B10) for the negative harmonic. Positive higher order harmonics are subsequently calculated using $R_Q = -C_Q R_{Q-1}$ and the negative harmonics from $R_{-Q} = -G_{-Q} R_{-Q+1}$.

The atomic polarization at ω_1 is proportional to the fourth element of R_0 and the fifth element of R_1 [see Eq. (3)]. The atomic polarization at ω_2 is proportional to the fifth element of R_0 and the fourth element of R_{-1}. The atomic polarization of the anti-Stokes signal is proportional to the fourth element of R_1 and that of the Stokes signal to the fifth element of R_{-1}. The ground state coherence is proportional to σ_{ba} (third element of R_0).

[1] E. Arimondo, *Progress in Optics XXXV* (Elsevier Science B.V., Amsterdam, 1996), Vol. 5.
[2] G. Alzetta, A. Gozzini, L. Moi, and G. Orriols, Nuovo Cimento B **36**, 5 (1976).
[3] H. Gray, R. Whitley, and C. Stroud, Jr., Opt. Lett. **3**, 218 (1978).
[4] S. Harris, J. Field, and A. Imamoğlu, Phys. Rev. Lett. **64**, 1107 (1990).
[5] S. Tewari and G. Agarwal, Phys. Rev. Lett. **56**, 1811 (1986).
[6] Y. Li and M. Xiao, Opt. Lett. **21**, 1064 (1996).
[7] M. Jain, H. Xia, G. Yin, A. Merriam, and S. Harris, Phys. Rev. Lett. **77**, 4326 (1996).
[8] E. Mikhailov, Y. Rostovtsev, and G. Welch, J. Mod. Opt. **49**, 2535 (2002).
[9] E. Mikhailov, I. Novikova, Y. Rostovtsev, and G. Welch, quant-ph/030917.
[10] A. Aspect, E. Arimondo, R. Kaiser, N. Vansteenkiste, and C. Cohen-Tannoudji, Phys. Rev. Lett. **61**, 826 (1988).
[11] L. Hau, S. Harris, Z. Dutton, and C. Behroozi, Nature (London) **397**, 594 (1999).
[12] M. Kash, V. Sautenkov, A. Zibrov, L. Hollberg, G. Wlech, M. Lukin, Y. Rostovtsev, E. Fry, and M. Scully, Phys. Rev. Lett. **82**, 5229 (1999).
[13] R. Wynands and A. Nagel, Appl. Phys. B: Lasers Opt. **68**, 1 (1999).
[14] J. Thomas, S. Ezekiel, C. Leiby, Jr., R. Picard, and C. Willis, Opt. Lett. **6**, 298 (1981).
[15] S. Knappe, R. Wynands, J. Kitching, H. Robinson, and L. Hollberg, J. Opt. Soc. Am. B **18**, 1545 (2001).
[16] A. Akulshin, S. Barreiro, and A. Lezama, Phys. Rev. A **57**, 2996 (1998).
[17] A. Lezama, S. Barreiro, A. Lipsich, and A. Akulshin, Phys. Rev. A **61**, 013801 (1999).
[18] C. Goren, A. Wilson-Gordon, M. Rosenbluh, and H. Friedmann, Phys. Rev. A **67**, 033807 (2003).
[19] A. Zibrov, C. Ye, Y. Rostovstev, A. Matsko, and M. Scully, Phys. Rev. A **65**, 043817 (2002).
[20] C. Ye, A. Zibrov, Y. Rostovtsev, A. Matsko, and M. Scully, J. Mod. Opt. **49**, 2485 (2002).
[21] A. Akulshin, A. Cimmino, A. Sidorov, P. Hannaford, and G. Opat, Phys. Rev. A **67**, 011801 (2003).
[22] S. Babin, D. Churkin, E. Podivilov, V. Potapov, and D. Shapiro, Phys. Rev. A **67**, 043808 (2003).
[23] M. Levenson, *Introduction to Nonlinear Laser Spectroscopy* (Academic, New York, 1982).
[24] N. Bloembergen, Am. J. Phys. **35**, 989 (1967).
[25] Y. Shen, in *Light Scattering in Solids*, edited by M. Cardona, Topics in Applied Physics, Vol. 8 (Springer-Verlag, Berlin, 1975), p. 275.
[26] M. Levenson and J. Song, in *Coherent Nonlinear Optics*, edited by M. Feld and V. Letokhov, Topics in Current Physics, Vol. 21 (Springer-Verlag, Berlin, 1980), p. 293.

[27] E. Woodbury and W. Ng, Proc. IRE **50**, 2367 (1962).
[28] P. Maker and R. Terhune, Phys. Rev. **137**, A801 (1965).
[29] J. Nibler and G. Knighten, in *Raman Spectroscopy of Gases and Liquids*, edited by A. Weber, Topics in Current Physics, Vol. 11 (Springer-Verlag, Berlin, 1978), Chap. 7, p. 253.
[30] J. Shirley, R. Hall, and A. Eckbreth, Opt. Lett. **5**, 380 (1980).
[31] D. Rousseau, J. Friedman, and P. Williams, in *Raman Spectroscopy of Gases and Liquids*, edited by A. Weber, Topics in Current Physics, Vol. 11 (Ref. [29]), Chap. 6, p. 203.
[32] L. Allen and J. Eberly, *Optical Resonance and Two-Level Atoms* (Wiley, New York, 1975).
[33] V. Wong, R. Boyd, C. Stroud, Jr., R. Bennink, and A. Marino, Phys. Rev. A **68**, 012502 (2003).
[34] S. Papademetriou, S. Chakmakjian, and C. R. Stroud, Jr., J. Opt. Soc. Am. B **9**, 1182 (1992).